An assessment of models for flow-enhanced nucleation in an n-alkane melt by molecular simulation

An assessment of models for flow-enhanced nucleation in an *n*-alkane melt by molecular simulation

David A. Nicholson and Gregory C. Rutledge

Department of Chemical Engineering, Massachusetts Institute of Technology,

Cambridge, MA 02139

Abstract

Flow-enhanced nucleation of the crystal phase under shear and uniaxial extension for a monodisperse melt of *n*-pentacontahectane ($C_{150}H_{302}$, or C150) chains was studied by non-equilibrium molecular dynamics (NEMD) simulation. The resulting acceleration in the crystal nucleation rate was correlated with macroscopically measurable properties of the flow field and with microscopic conformational statistics. Based on the fidelity of the observed correlations, several empirical models reported in the literature were evaluated for their abilities to account for the observed enhancement of the nucleation rate due to flow, and new models are proposed for data that do not comport with existing models. In agreement with prior reports, the nucleation rate was found to correlate well with first normal stress difference, the second invariant of the deviatoric conformation tensor, and the stretch ratio, albeit with some differences from the existing models. New models based on conformational invariants for Kuhn segments are proposed, and shown to describe the simulation data more accurately than those based on conformational behavior of entire chains. Within the applicability of the stress-optical rule, related models are proposed based on invariants of the extra stress tensor.

Introduction

When a flow field is applied to a polymer melt, its constitutive chains may stretch and orient. For polymers that undergo crystallization, the extent to which stretching and orientation takes place has a dramatic effect on the rate at which crystallization occurs. It is often possible to

construct a rheological model for the effect of an applied flow field on chain conformations [1,2]. Similarly, if the kinetic rates associated with crystallization are known empirically, it is a relatively straightforward task to determine the evolution of crystalline morphology in a material [3,4]. It is not straightforward, however, to determine how changes in chain conformations influence crystallization rates, or how the development of a multi-phase structure affects the evolution of chain conformations under flow. Understanding these two relationships is the most challenging hurdle that researchers face when developing models for flow-induced crystallization (FIC).

In this work, we consider the early stage of the crystallization process during flow, sometimes referred to as flow-enhanced nucleation (FEN). In this regime, it suffices to consider only how the response of the melt to the flow field affects the rate of crystal nucleation. There have been a number of investigations into this topic, typically involving a combination of experiments and modeling [5,6]. It has been suggested that the nucleation rate depends variously on strain rate [7,8], stress response [9–11], chain conformations [12–14], and flow-induced free energy [15]. In the Appendix, an index is provided of the FEN models referenced in this study, organized by these four classes. The reason for the quantity and variety of these relationships lies in the difficulty associated with performing experiments to discriminate among them. Nucleation occurs at a small spatiotemporal scale, making it difficult to measure its rate directly [16]. This is especially true for the accelerated rates associated with strong flow fields. Additionally, it is not straightforward to measure all aspects of the response of a material to flow, often requiring researchers to rely on rheological models.

Molecular simulation, on the other hand, does not suffer from these difficulties. It is possible to observe nucleation directly and to measure accurately its rate [17–19]. Furthermore, there is no ambiguity in measuring the response to the flow field, given the complete configurational and energetic description that molecular models provide. These qualities have inspired a number of molecular simulation studies of flow-induced crystallization [6,20], although relatively few that focused on nucleation kinetics [14,21,22]. Of these, only the coarse-grained kinetic Monte Carlo study by Graham and Olmsted [14] was undertaken with the objective of drawing correlations between the nucleation rate and the response of a polymer to an applied flow field.

In this study, we use the non-equilibrium molecular dynamics (NEMD) method to observe nucleation and compute its rate under various conditions of flow field and strain rate. Factors that characterize the response of the melt to the applied flow field are drawn from the literature or formulated a priori, and their correlations with the nucleation rate evaluated and compared critically, given the resulting data for molecular conformations, field strengths and clustering kinetics. In this way, the better models and their associated physical interpretations can be validated to some extent, and new models can be proposed when existing models are found to be inadequate. We believe that these results may serve to guide future efforts to construct crystallization models that bridge the gap between melt rheology and crystallization kinetics.

Methods

The simulations were performed with a monodisperse melt composed of 100 linear *n*-pentacontahectane ($C_{150}H_{302}$, or C150) chains. This chain length was chosen because it is approximately twice the segment length of 60–90 carbons [23–26] between entanglements in polyethylene; it reflects a trade-off between chain length and simulation time. The *n*-alkane chains were modeled using a realistic united atom (UA) representation for each CH_2 or CH_3 group. The force field used was initially proposed by Paul et al. [27], and includes subsequent modifications from Waheed *et al.* [28,29]. It includes terms for bond stretching, angle bending, torsion, and non-bonded Lennard-Jones interactions. The functional forms and parameters for these terms are reproduced in Table S1 of the Supplementary Material.

Simulations under steady-state shear and uniaxial extension were performed by integrating the SLLOD equations of motion [30] and applying the appropriate boundary condition for the type of flow field. For shear flow, the Lagrangian Rhomboid boundary condition [31] was used, which has been shown to be equivalent to the Lee-Edwards sliding brick condition [32,33]. For uniaxial extension, the boundary condition from Dobson [34] was used, along with numerical lattice reduction as proposed by Hunt [35]. All simulations were carried out in LAMMPS [36]. The implementation of the Hunt-Dobson boundary conditions from the USER-UEF package [22] was used for the extensional flow fields. For both types of boundary conditions the initial simulation box, $\mathbf{H}_0$, was cubic, with an average side length of 7.5 nm (density $\rho = 0.83$ g/cc) at T = 440 K. In shear, $\mathbf{H}_0$ is coaxial with the coordinate frame of the

applied shear. In extension, $\mathbf{H}_0$ is rotated with respect to the coordinate frame of the applied flow field according to the condition identified by Dobson [34]. A constant true strain is applied according to the rate-of-deformation tensor $\boldsymbol{\nabla}\mathbf{u}$, leading to a simulation box that evolves with times as $\mathbf{H}(t) = \mathbf{H}_0 \cdot \exp(\boldsymbol{\nabla}\mathbf{u}\, t)$. As the simulation proceeds, the simulation box becomes elongated, requiring regular remapping to equivalent simulation boxes that are less elongated, through a lattice reduction method. Additional details about this procedure can be found in Hunt [35], Dobson [34] and Nicholson and Rutledge [22].

The external pressure, P_{ext}, was set to 1 atm through a constant stress condition applied in directions corresponding to free surfaces in laboratory flows. For shear, the vorticity direction corresponds to a free surface. For uniaxial extension, the two compression directions correspond to free surfaces. The stress condition was achieved by scaling the simulation box isotropically in order to control the average stress in all free surface directions to P_{ext}. Under this scheme, the total strain applied to the simulation box has a volume-preserving contribution from the applied flow field and a non-volume-preserving contribution due to the stress condition. Under steady-state flow, where the average density is not changing, the non-volume-preserving contribution to the strain will fluctuate around an average value. In this case, the average strain rate associated with the pressure control scheme averages out to zero, leaving only the volume-preserving contribution to the strain rate from the applied flow field. All simulations were performed using the LAMMPS implementation of the Nose-Hoover thermostat and barostat, with time constants of 0.4 ps and 4 ps, respectively. The equations of motion were integrated using an rRESPA [37] scheme with a 2 fs time step for bonded interactions and a 4 fs time step for nonbonded interactions.

In order to simulate nucleation under steady-state flow, an 840 ns equilibration trajectory was first performed at 440 K under constant strain rate for each flow condition. From the last 750 ns of each equilibration trajectory, 25 snapshots were selected in increments of 30 ns to serve as initial conditions for nucleation runs. This time increment is roughly equal to the Rouse time τ_R of the C150 melt at 440 K, thus ensuring that starting configurations for nucleation runs are essentially independent. Nucleation runs were performed by quenching the temperature to 280 K, while simultaneously reducing the strain rate $\dot{\gamma}$ in a manner such that the Weissenberg number, $\mathrm{Wi} = \dot{\gamma}\tau_R$, remained constant through the quench. This procedure was chosen in order to reduce

the transient adjustment of the melt to the quench temperature during the nucleation runs. The Rouse times at the equilibration and crystallization temperatures were obtained from the τ_R vs. $1/T$ data reported in Fig. 2a (inset) of Yi and Rutledge [38] by interpolation between the two nearest temperature points. At 280 K, τ_R = 340 ns, and at 440 K, τ_R = 26 ns. The crystallization temperature corresponds to 29% supercooling, based on the experimental melting temperature of C150, T_m = 396.4 [39]. This supercooling is deep relative to typical experimental values, but is necessary to observe nucleation at slow strain rates that approach the quiescent condition. At this supercooling, the quiescent critical nucleus size is small compared to the entanglement length [38], and an applied flow field further reduces the size of the nucleus [22]. For shallower supercooling and weak flow conditions, the critical nucleus size is expected to be larger, and may approach the entanglement length, at which point there may be an additional effect associated with the onset of entanglement dynamics in nucleation, as discussed by Yi and Rutledge [38]; by using deep supercooling, this effect was avoided in our simulations.

As nucleation proceeded, crystalline clusters were identified based on nematic order using a method outlined in a previous study [22], based in turn on the one proposed by Yi and Rutledge [40]. In the current study, the threshold value for the local nematic order was set to $P_{2,\mathrm{tr}}$ = 0.7, compared to $P_{2,\mathrm{tr}}$ = 0.52 used in the prior study of *n*-eicosane (C20) [22]. The larger value was necessary to discriminate crystalline UAs from noncrystalline ones in flow, due to the high level of local orientational order already exhibited by C150 in the melt state for the range of strain rates under study. From the results of the clustering method, the transient evolution of the largest cluster $n_{\mathrm{largest}}(t)$ was computed for each crystallization run and used to compute the first-passage time for the largest cluster $T_{\mathrm{largest}}(n) = \min\left(t \middle| n_{\mathrm{largest}}(t) \geq n\right)$. Nucleation rates were computed using the analysis method originally proposed by Shneidman [17], wherein it is assumed that $T_{\mathrm{largest}}(n)$ obeys a shifted exponential distribution. From a set of crystallization runs, the standard deviation of $T_{\mathrm{largest}}(n)$, $\sigma_{\mathrm{largest}}(n)$, was computed. $\sigma_{\mathrm{largest}}(n)$ is constant at large values of n, even as the mean of the distribution $\tau_{\mathrm{largest}}(n)$ is increased due to transients and post-critical cluster growth. The nucleation rate can then be computed from $I_S = \left(V\sigma_{\mathrm{plateau}}\right)^{-1}$, where V

is the volume of the simulation box and $\sigma_{\text{plateau}}(n) = \left\langle \sigma_{\text{largest}}(n) \right\rangle_{150<n<300}$. Additional details about this procedure can be found in Shneidman [17] and Nicholson and Rutledge [22].

Results and discussion

In this section, we report assessments of FEN models listed in the Appendix. Experimental procedures and additional features of the models such as growth rates, saturation effects, and rheological models are not discussed. For a more detailed overview of these features, we direct readers to reviews by Peters et al. [5] and Graham [6] . In some cases, the models invoke a constant nucleation density, N_q, for the quiescent melt (typical of heterogeneous nucleation), rather than a constant nucleation rate $I_{S,q}$ (typical of homogeneous nucleation). In this analysis, we focus exclusively on homogeneous nucleation, as prescribed by the simulations, with constant $I_{s,q}$. Quantities that are referred to as constants in this section are independent of the applied flow field, but may depend on other conditions such as the temperature and hydrodynamic pressure. In each model $I_{S,q}$ appears as one such constant.

In order to evaluate FEN models from the literature, averages of relevant properties of the melts, such as stresses and configurational metrics, are taken from the equilibration runs for each flow condition at 440 K. Each crystallization run takes place at the same Wi as its associated equilibration run, so that configurational metrics and their contributions to the stress are minimally affected by the change in temperature; across all flow conditions, the average end-to-end distance over the first 5 ns of the crystallization runs is within 5% of the average value from the equilibration run. The correlation of relevant melt properties with the nucleation rate is evaluated and, where good correlation is observed, fits are performed to model expressions. Due to the large range over which the nucleation rate varies, non-linear least squares fits were performed to the logarithm of the nucleation rate. The quality of fit associated with a given expression is reported using the sum of log residuals, henceforth referred to as residual, which is the objective function of the fit.

Assessment of strain rate-based FEN models

For the purpose of comparing results under shear and extension, the strain rate is defined as $\dot{\gamma} = \sqrt{J_2(\mathbf{D})/2}$, where the strain rate tensor is given by $\mathbf{D} = \nabla\mathbf{u} + (\nabla\mathbf{u})^t$, and $J_2(\mathbf{A}) = \mathrm{tr}\left(\mathbf{A}^2\right)$ is the second invariant of tensor **A**. Employing this definition, a melt under flow has the same isothermal rate of energy dissipation at a given value of $\dot{\gamma}$, or equivalently Wi, under both shear and extension in the Newtonian limit [30]. The dependence of the nucleation rate on Wi is shown for the monodisperse melt in Fig. 1. When the melt is subjected to strain rates with Wi < 1, I_S is observed to correlate well with Wi. This result suggests that, in the absence of viscoelastic effects, the acceleration of the nucleation rate depends on the flow-induced rate of energy dissipation. For strain rates corresponding to Wi > 1, the nucleation rates for the monodisperse melt under shear and extension diverge, with a more rapid acceleration observed for extensional flow.

Several FEN models depend only on the evolution of the macroscopic geometry of the melt as prescribed by $\dot{\gamma}$. The model from Liedauer et al. [7], and used also by Isayev et al. [41,42], has a quadratic dependence of I_S on the strain rate,

$$I_S = I_{S,q} + \alpha_L \dot{\gamma}^2 \,, \tag{1}$$

where α_L is a constant pre-factor. Under steady-state flow, the model from Guo et al. [8] also depends only on $\dot{\gamma}$ according to,

$$I_S = I_{S,q} + \alpha_G \frac{\beta_G \dot{\gamma}^{\nu_G}}{1 + \beta_G \dot{\gamma}^{\nu_G}} \,, \tag{2}$$

where α_G, β_G and ν_G are constants. The divergence between extension and shear, observed in Fig. 1, implies that the strain rate alone is not a sufficient factor for correlating nucleation kinetics with an applied flow field in the viscoelastic regime, where Wi > 1. Relationships for the nucleation rate that do not include this viscoelastic response, including Eqs. (1) and (2), consequently fail to describe the results analyzed herein.

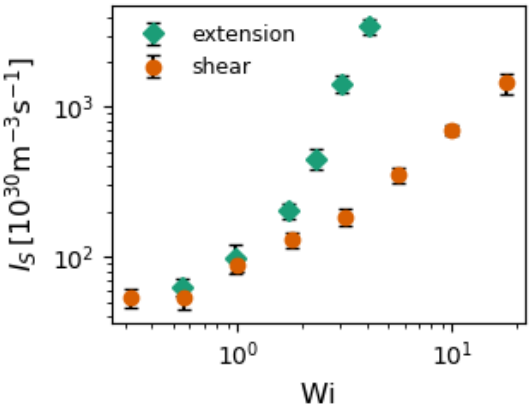

Figure 1 The NEMD nucleation rate as a function of the Weissenberg number for the C150 melt. The standard error in the nucleation rate was computed using the jackknife resampling technique.

Assessment of stress-based FEN models

Polymer chains respond to strong flows by stretching and orienting. At the macroscopic scale, stretch and orientation manifest themselves as anisotropy of the stress tensor. Following this line of thought, some researchers have constructed FEN models based on the development of stresses under flow. Using arguments from classical nucleation theory, Ziabicki [9] derived a flow-enhanced nucleation rate based on the first-normal stress difference, $N_1 = \sigma_{xx} - \sigma_{yy}$, where x is the flow direction and y is the gradient direction in shear or the radial compression direction in extension:

$$I_S = I_{S,q} \exp\left(\theta_{Z1} N_1^2\right). \tag{3}$$

In this expression, θ_{Z1} is a constant. The model from Koscher and Fulchiron [10] also relates the FEN contribution to N_1, but with a linear dependence,

$$I_S = I_{S,q} + \theta_{KF} N_1, \tag{4}$$

where θ_{KF} is a constant. Using the Irving-Kirkwood formula for the stress tensor [43], the NEMD dependence of I_S on N_1 is shown in Fig. 2a along with fitted curves to Eqs. (3) and (4). It appears that the $I_S \propto e^{N_1^2}$ dependence of Eq. (3) is too strong to model accurately the NEMD

data, whereas the $I_S \propto N_1$ dependence of Eq. (4) is too weak. In Fig. 2, we also include a new model expression,

$$I_S = I_{S,q} \exp(\theta_{M1} N_1), \tag{5}$$

where θ_{M1} is a fitting parameter. Of the three models shown, Eq. (5) is the most consistent with the trend of the data. This consistency is corroborated by the residuals for the different models, which are shown in the Appendix along with the fitting parameters.

In Eq. (5), the inverse of the fitting parameter, θ_{M1}^{-1} = 3.92 MPa, can be considered as a critical first-normal stress difference for the onset of flow-enhanced nucleation. The quiescent C150 nucleation rate, $I_{S,q}$ = 47.4×10^{30} m^{-3}s^{-1}, is roughly three times as large as the value reported by Yi and Rutledge [38], $I_{S,q}$ = 14.7 ×10^{30} m^{-3}s^{-1}, and roughly seven times as large as the value reported by Anwar et al. [21], 7.2 ×10^{30} m^{-3}s^{-1}. We attribute the small nucleation rates obtained in the previous studies to the overly large time steps used. Yi and Rutledge used a time step of 5 fs and Anwar et al. used a timestep of 5.26 fs, both of which are less accurate than the rRESPA scheme used in this study. In our previous study on C20 [19], we similarly observed that larger nucleation rates were obtained when the more accurate integration scheme was used. Additionally, use of the NVT ensemble by Anwar et al. may account for the lower nucleation rate observed there, compared to the NPT ensemble used by Yi and Rutledge and in this study, due to the extra dilatational stresses that accompany the changes of density associated with nucleation.

Another stress-based FEN relationship was introduced in the microstructural model for flow-induced crystallization by Doufas et al. [11], and used in subsequent studies by Doufas and co-workers [44–47]. This model is based on the trace of the extra stress tensor $\boldsymbol{\tau} = \boldsymbol{\sigma} - P_{\text{ext}}\mathbf{I}$, where P_{ext} = 1 atm is the stress applied by the barostat in directions corresponding to free surfaces. Unlike N_1, the trace of $\boldsymbol{\tau}$ is frame invariant and thus independent of the flow kinematics [11]. The model expression for the FEN rate is,

$$I_S = I_{S,q} \exp\left(\theta_D \, \text{tr}(\boldsymbol{\tau})\right), \tag{6}$$

where θ_D is a constant. The dependence of I_S on tr($\boldsymbol{\tau}$) for the NEMD results is shown in Fig. (2b). As was the case with Wi, the dependencies of I_S under shear and extension are non-overlapping, implying that Eq. (6) is not consistent with this study.

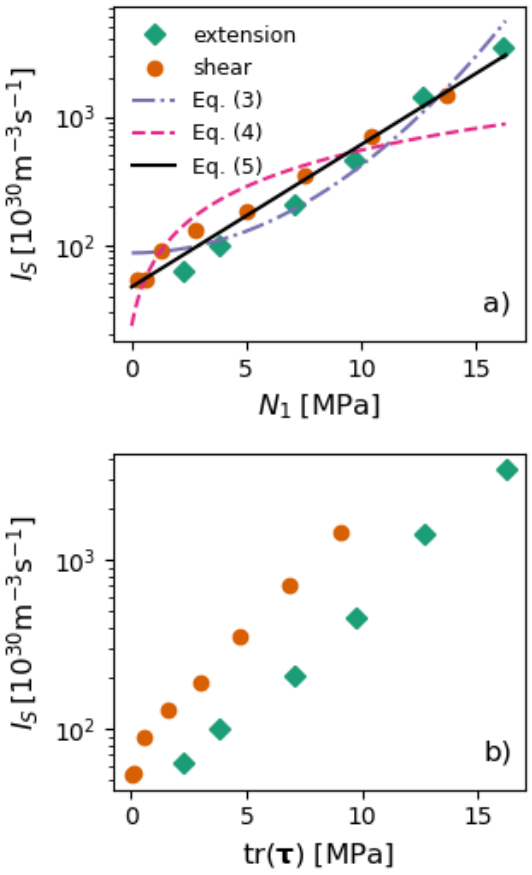

Figure 2 The NEMD nucleation rate as a function of (a) the first normal stress difference, and (b) the trace of the extra stress tensor. The curves correspond to fits to different FEN models; fitting results are shown in the Appendix.

Assessment of conformation-based FEN models

A number of FEN models have been constructed based on a presumed dependence of the nucleation rate on chain conformations. In the recoverable strain model introduced by Zuidema et al. [12], and used in subsequent studies by Peters and co-workers [48–50], the nucleation rate due to flow is related to the second invariant of the deviatoric elastic finger tensor, $\mathbf{B}_d^e$ for a

representative mode in a multimode rheological model. For a given mode, the elastic finger tensor is proportional to the average conformation tensor, $\mathbf{C} = \langle \mathbf{RR} \rangle / R_0^2$, for the associated chain segment length [51,52], where $\mathbf{R}$ is the end-to-end segment vector and R_0 is its equilibrium length. In terms of the conformation tensor, the flow-enhanced nucleation rate for this model is,

$$I_S = I_{S,q} + \theta_{Z2} J_2 \left(\mathbf{C} - \mathbf{I} \frac{\mathrm{tr}(\mathbf{C})}{3} \right), \tag{7}$$

where θ_{Z2} is a constant. Taking the slowest Rouse mode for the chain as the representative mode for the C150 melt (i.e., $\mathbf{R}$ is the end-to-end distance for the entire chain), the dependence of I_S on the second invariant of the deviatoric conformation tensor is shown in Fig. 3a. The fit to Eq. (7) is shown also in Fig. 3a, and the fitting results are given in the Appendix. The FEN effect correlates well with the invariant quantity, and the correlation is described well by the form of Eq. (7). Based on the residual, the fit is similar in quality to Eq. (5) and yields a comparable value for $I_{S,q}$.

For a given segment length, the conformation tensor can be decomposed into contributions due to the stretch ratio, $\lambda = \sqrt{\mathrm{tr}(\mathbf{C})}$, and the orientation tensor $\mathbf{S}$, according to, $\mathbf{C} = \lambda^2 \mathbf{S}$. The orientation tensor is related to the nematic order tensor, $\mathbf{P}_2$, by, $\mathbf{P}_2 = 1/2\ (3\mathbf{S} – \mathbf{I})$. Eq. (7) can be rewritten [5] in terms of the contributions from λ and $\mathbf{P}_2$, as follows:

$$I_S = I_{S,q} + \frac{4}{9} \theta_{Z2} \lambda^4 J_2 (\mathbf{P}_2). \tag{8}$$

In the model introduced by Steenbakkers et al. [13], and used in various studies by Peters and co-workers [51,53–55], the enhancement of nucleation due to flow was ascribed solely to the dependence on stretching, rather than the combination of stretching and orientation that is implicit in Eq. (7), and explicit in Eq. (8). The expression of Steenbakkers et al. was,

$$I_S = I_{S,q} + \theta_S (\lambda^4 - 1), \tag{9}$$

where θ_S is a constant pre-factor. Steenbakkers and Peters [51] found that Eq. (9) provided a better description of their experimental data than an expression in which the enhancement in

nucleation rate due to flow was assumed to be proportional to the orientation contribution, $J_2(\mathbf{P}_2)$. This observation was taken as an indication that the success of prior studies using Eq. (7), or equivalently Eq. (8), was due to the stretch ratio contribution. Using kinetic Monte Carlo simulation, Graham and Olmsted [14] corroborated the use of Eq. (9) for stretch ratios less than 3.5, and found that an exponential expression was consistent with their data over a wider range of strain rates,

$$I_S = I_{S,q} \exp\left[\theta_{GO}\left(\lambda^2 - 1\right)\right], \tag{10}$$

where θ_{GO} is a constant pre-factor. Moreover, using a modified Giesekus model for the melt component in blown film simulations, Doufas [47] observed a correlation between the trace of the dimensionless extra stress tensor, used in Eq. (6), and the argument based on stretch ratio in Eq. (10), suggesting that the two equations capture the same physics, at least for that model.

Again using the end-to-end distance of the entire C150 chain as the representative segment length, the NEMD dependence of I_S on λ is shown in Fig. 3b along with fits to Eqs. (9) and (10). The nucleation rate is found to correlate well with the stretch ratio, and Eq. (9) is found to model the trend well. Eq. (10), on the other hand, is not a good fit for the NEMD results. This observation is corroborated by the residuals, which are shown in the Appendix along with fitted parameters for each model. Based on its residual, the fit to Eq. (9) is of similar quality to fits for Eqs. (5) and (7), and its value for $I_{S,q}$ is comparable to the values obtained from those two models.

The results of this section are surprising, given that Eq. (9) was originally developed as an improvement [56] upon Eq.(7), and Eq. (10) was previously reported to be a more accurate [14] expression than Eq. (9). By contrast, we find that Eqs. (7) and (9) perform similarly well, and Eq. (10) performs poorly for our NEMD data. In Fig. 3b, the NEMD data indicate a dependence of log (I_S) on λ that is clearly concave, while Eq. (10) implies a dependence that is convex for all λ. A closer look at Eq. (9) reveals that convexity of log (I_S) versus λ depends on the parameter values. When $I_{S,q}/\theta_S < 4/3$, log (I_S) is concave for all λ. When $I_{S,q}/\theta_S > 4/3$, log (I_S) is convex for $\lambda < \lambda_c$ and concave for $\lambda > \lambda_c$, where $\lambda_c = \left[3\left(I_{S,q}/\theta_S\right) - 1\right]^{1/4}$. For the NEMD data, $I_{S,q}/\theta_S = 0.31 < 4/3$, whereas the extraction of parameters from the master curve reported by

Graham and Olmsted [14] yields the value $I_{S,q}/\theta_S = 14 > 4/3$. Within the framework of Eq. (9), this analysis indicates that the strength of the flow-enhancement effect, as quantified by the value of θ_S relative to $I_{S,q}$, is responsible for the different logarithmic convexities of I_S between the two studies. Furthermore, the similarity between Eqs. (9) and (10) at small values of λ reported by Graham and Olmsted is only valid for certain parameterizations of Eq. (9).

The reason behind this incongruity is unclear, but we suspect that it may be attributable to the comparatively short chains used in this NEMD study. Graham and Olmsted [14] modeled chains with entanglement strands of length $N_K = 100$ Kuhn segments, whereas the model employed here is atomistic in resolution but with a length of only 150 carbons (about $N_K = 12$–13 Kuhn segments). Assuming Gaussian statistics in the absence of flow, full extension corresponds to a stretch ratio of $\sqrt{N_K}$. In Graham and Olmsted's study, $\lambda = 10$ would correspond to full extension of entanglement strands, whereas $\lambda \approx 3.5$ corresponds to full extension of chains in this study. Despite the similar range in λ explored in the two studies, the NEMD chains are more closely approaching full extension. We postulate that the logarithmic concavity observed in Fig. 3 is a consequence of finite extensibility. Our expectation is that as chains become severely stretched, the nucleation rate will saturate, implying a concave dependence of I_S on λ for values of λ that approach full extension.

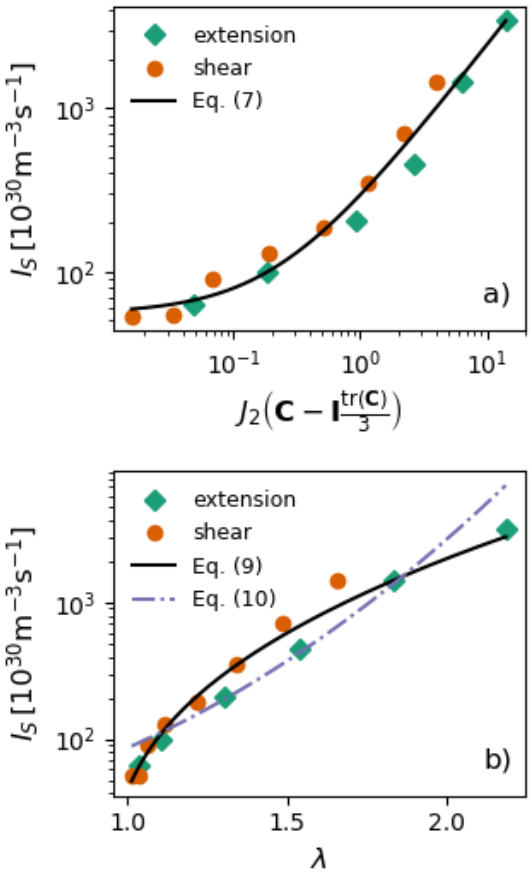

Figure 3 The NEMD nucleation rate as a function of (a) the second invariant of the deviatoric conformation tensor, and (b) the stretch ratio. The curves correspond to fits to different FEN models, with fitting results shown in the Appendix.

Assessment of free energy FEN models

When a melt is subjected to flow, it undergoes an increase in free energy, ΔG_f, due to chain stretching and orientation, which in turn increases the thermodynamic driving force for crystallization, $\Delta G = \Delta G_q + \Delta G_f$, where ΔG_q is the difference in free energy between melt and crystal in the absence of flow. If these free energies can be estimated, then the increase in isothermal steady state nucleation rate due to flow can be estimated within the framework of nucleation theory. This approach was used by McHugh [57,58] in early studies of FIC in solution. Using a nucleation expression from Ziabicki [59], the FEN rate takes the form

$$I_S = I_{S,q}\left(1+\frac{\Delta G_f}{\Delta G_q}\right)\exp\left[\frac{K}{T\left(\Delta G_q\right)^n}\left(1-\frac{1}{\left[1+\Delta G_f/\Delta G_q\right]^n}\right)\right], \tag{11}$$

where K is a constant and n = 1 or 2 for secondary or primary nucleation, respectively. This approach was taken by Coppola et al. [15], who used the Doi-Edwards model to estimate ΔG_f as a function of flow conditions. This approach has been used, with modification in some cases, in a number of other studies [60–63]. In a kinetic Monte Carlo study, Jolley and Graham [64] included a contribution from the change in elastic free energy arising from the reduction in entropy for a chain segment stretched in flow, from which they obtained semi-analytic results for the enhancement factor, $I_S/I_{S,q}$.

Estimates of ΔG_q and ΔG_f directly from molecular simulations require thermodynamic integration, such as that reported previously by Bernardin [65], using a semi-grand canonical Monte Carlo (SGMC) simulation to obtain the reversible (i.e. lower bound) work of orientation for chains of length C24 to C400 at 450 K. Such integrations were not conducted in the NEMD simulations performed here, but a rough evaluation of Eq. (11) is performed based on the relationship shown in Fig. 11 of [65], which exhibits a quadratic dependence of ΔG_f on the orientational order parameter for chord vectors $P_{2,C}$. Chord vectors are chain segments that are 3 UAs long, and $P_{2,C}$ is the largest eigenvalue of the nematic order tensor for chord vectors, $\mathbf{P}_{2,C}$. Under the assumption that this quadratic relationship is temperature-independent, ΔG_f can be replaced with $\mu P_{2,C}^2$ in Eq. (11), where μ is a constant. For ΔG_q, we use the value for ΔH = 467 ±17 kJ/mol for C150, reported by Yi et al. [38] and the usual relation, $\Delta G_q = \Delta H \Delta T / T_m$ = 137 kJ/mol, valid for shallow undercooling. Inserting these relationships into the primary nucleation (n = 2) form of Eq. (11) yields the following expression,

$$I_S = I_{S,q}\left(1+\frac{\mu P_{2,C}^2}{\Delta G_q}\right)\exp\left[\frac{K}{T\left(\Delta G_q\right)^2}\left(1-\frac{1}{\left[1+\mu P_{2,C}^2/\Delta G_q\right]^2}\right)\right]. \tag{12}$$

The NEMD data for I_S versus $P_{2,C}^2$ is shown in Fig. 4, along with the best fit to Eq. (12); the resulting parameter values and residual of the fit are given in the Appendix. The values of ΔG_f obtained from fitting, shown as the top axis in Fig. 4, are two orders of magnitude larger than the

values obtained by Bernardin at Rutledge [65]. Based on the large residual, Eq. (12) apparently does not describe the NEMD data well.

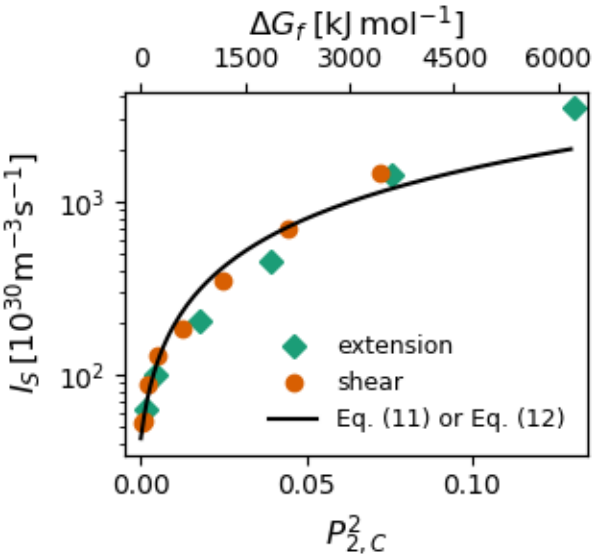

Figure 4 The NEMD nucleation rate as a function of the square of the nematic order parameter for chord vectors $P^2_{2,C}$. The solid line corresponds to a fit to Eq. (12) with fitting results shown in the Appendix. The flow-induced free energy resulting from the fit was is shown as the top axis. Based on this axis, the fitted curve corresponds to Eq. (11) with $n = 2$.

New FEN models based on Kuhn segments

During flow, stretching takes place over a range of length scales that correspond to different relaxation modes. In the conformation-based FEN models discussed thus far [12–14], the enhancement in nucleation rate due to flow is associated with stretching and orientation on the entanglement length scale. The flow-induced deformation of an entanglement strand involves the reorientation of its constitutive Kuhn segments [66]. Theoretical studies have established relationships between chain deformation and Kuhn segment orientation [67,68]. From a kinetic perspective, it is reasonable to consider that nucleation occurs more readily when Kuhn segments are already co-aligned in the melt, due to flow for example. Following this line of reasoning, we next examined the dependence of the flow-enhanced nucleation rate on Kuhn segment

conformations, represented by the Kuhn segment conformation tensor, $\mathbf{C}_K = \langle \mathbf{R}_K \mathbf{R}_K \rangle / R_{K,0}^2$, where the subscript *K* is used to indicate explicitly that the Kuhn segment is the length scale used. For polyethylene, the Kuhn segment corresponds to 12 UAs, and the brackets denote an average over all segments that are 12 UAs long.

The dependence of the flow-enhanced nucleation rate on the second invariant of the deviatoric conformation tensor, $J_2\left(\mathbf{C}_K - \mathbf{I}\,\mathrm{tr}\left(\mathbf{C}_K\right)/3\right)$, is studied along with its separate contribution [5] due to orientation, $J_2(\mathbf{P}_{2,K})$, where $\mathbf{P}_{2,K} = 1/2\left[3\mathbf{C}_K / \mathrm{tr}\left(\mathbf{C}_K\right) - \mathbf{I}\right]$. These dependencies are shown in Figs. 5a and 5b. respectively. Due to the short segment length, the observed variation in λ_K is rather small (<6%), and may be ignored. Each quantity shows good correlation with the nucleation rate; qualitatively, the correlations appear to be of higher fidelity than those shown in Figs. 1-4. The dependencies of I_S on $J_2\left(\mathbf{C}_K - \mathbf{I}\,\mathrm{tr}\left(\mathbf{C}_K\right)/3\right)$ and $J_2(\mathbf{P}_{2,K})$ are similar, and are consistent with the following relationships,

$$I_S = I_{S,q} \exp\left[\theta_{M2}\sqrt{J_2\left(\mathbf{C}_K - \mathbf{I}\frac{\mathrm{tr}\left(\mathbf{C}_K\right)}{3}\right)}\right], \tag{13a}$$

$$I_S = I_{S,q} \exp\left[\theta_{M3}\sqrt{J_2\left(\mathbf{P}_{2,K}\right)}\right], \tag{13b}$$

where θ_{M2} and θ_{M3} are constants. Based on Eq. (8), the similarity between Figs. 5a and 5b implies that it is the orientation of Kuhn segments induced by flow, rather than stretching of those segments (which as previously noted is quite minor), that accounts for the FEN effect.

The fitting results for Eqs. (13a) and (13b), shown in the Appendix, indicate a higher quality of fit than those obtained using the previously discussed FEN models. The values θ_{M2}^{-2} = 0.0166 and θ_{M3}^{-2} = 0.0298 can be interpreted as critical values for their respective second invariants corresponding to the onset of FEN. The values of $I_{S,q}$ agree reasonably well with values obtained from other models in this study. Under the condition of uniaxial symmetry about the primary axis of orientation, the quantity $\sqrt{J_2(\mathbf{P}_{2,K})}$ that appears in Eq. (13b) is proportional to the Kuhn segment nematic order parameter, $P_{2,K}$., which can be estimated by some rheological models and is accessible experimentally via the birefringence [68]. The dependence of I_S on $P_{2,\mathrm{K}}$,

computed as the largest eigenvalue of $\mathbf{P}_{2,K}$, is shown in Fig. 5c. An exponential dependence is observed, corresponding to the relationship,

$$I_S = I_{S,q} \exp\left(\theta_{M4} P_{2,K}\right), \tag{14}$$

where θ_{M4} is a constant. This observation suggests that the reorientation of Kuhn segments is approximately uniaxial about the largest principal axis of $\mathbf{P}_{2,K}$ for both shear and extension. The fitting results are shown in the Appendix, wherein the quantity $\theta_{M4}^{-1} = 0.142$ can be considered to be a critical value for $P_{2,K}$ demarcating the onset of FEN.

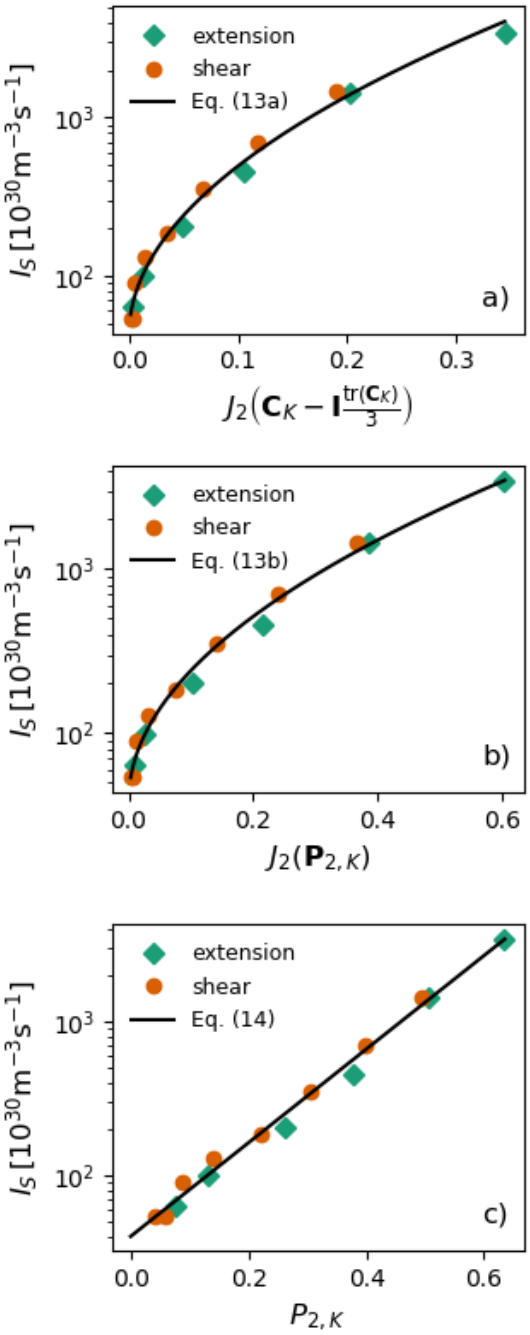

Figure 5 The NEMD nucleation rate as a function of (a) the second invariant of the deviatoric Kuhn segment conformation tensor, (b) the Kuhn segment nematic order tensor and (c) the Kuhn segment nematic order parameter. The curves correspond to fits to different FEN models, with fitting results in the Appendix.

Interestingly, a comparison of Eqs. (5) and (14) indicates that I_S depends on the first normal stress difference, N_1, in the same way that it depends on the Kuhn segment nematic order parameter $P_{2,K}$, consistent with the stress-optical rule. Within the framework of the stress-optical rule [69], the extra stress tensor, $\boldsymbol{\tau}$, is coaxial with the nematic order parameter tensor $\mathbf{P}_{2,K}$. This coaxiality is demonstrated in Fig. 6a by a linear relationship between the largest principal extra stress, $\tau^{(1)}$, and $P_{2,K}$. The adherence of this model system to the stress-optical rule was also observed for various alkane chain lengths using SGMC by Bernardin and Rutledge [65]. Given that the correlations based on $\mathbf{P}_{2,K}$ were found to be of higher fidelity than the stress models listed in the Appendix, the adherence to the stress-optical rule indicates promise for new FEN models based on the extra stress tensor. For systems that obey the stress optical rule, we expect that these models will prove to be useful in cases where the Kuhn segment orientation data are not available, but stress data are. By substitution of $\boldsymbol{\tau}$ for $\mathbf{P}_{2,K}$, in Eq. (13b), and $\tau^{(1)}$ for $\boldsymbol{\tau}$ in Eq.(14), we propose the following relationships,

$$I_S = I_{S,q} \exp\left[\theta_{M5}\sqrt{J_2(\boldsymbol{\tau})}\right], \tag{15a}$$

$$I_S = I_{S,q} \exp\left[\theta_{M6}\tau^{(1)}\right], \tag{15b}$$

where θ_{M5} and θ_{M6} are constants. As is shown in Fig. 6, these relationships are consistent with the NEMD data, and the fitting results, shown in the Appendix indicate a higher quality of fit than the other stress-based models.

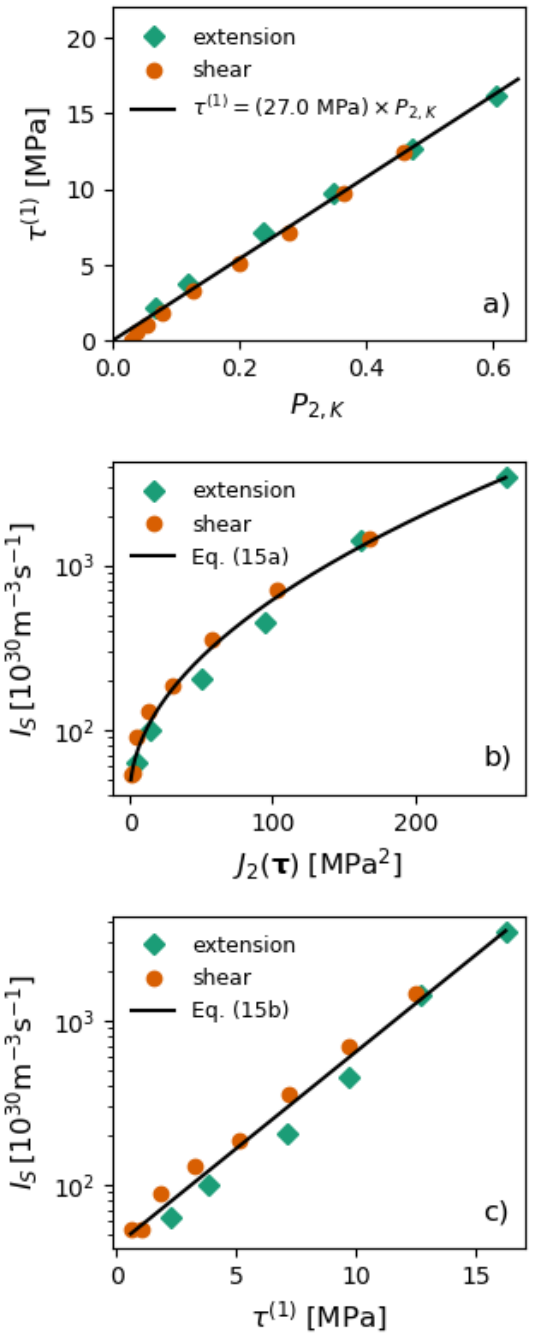

Figure 6 (a) The stress-optical rule, as indicated by the proportionality of the first principal extra stress and the Kuhn segment nematic order tensor. (b) The NEMD nucleation rate as a function of the second invariant of the extra stress. (c) The NEMD nucleation rate as a function of the first principal extra stress. The curves correspond to fits to different FEN models, with fitting results in the Appendix.

Summary and conclusions

Due to its fine spatiotemporal resolution and the capability to characterize completely the systems under study, NEMD is a useful technique for investigating the relationship between the response of a polymer material to an applied flow field and the resulting effect on nucleation kinetics. By selecting nucleation rate expressions from the literature and examining their consistency with the results obtained, the method offers insight into which forms are promising candidates for the construction of models for FEN kinetics. We demonstrate that accurate FEN models exist on both the macroscopic or microscopic scale. For the majority of cases, only the quiescient nucleation rate and one empirical parameter are required to model nucleation kinetics under isothermal conditions.

Based on our assessments, we find that flow conditions that lead to similar changes in chain conformations lead to similar nucleation rates. The unifying feature of the better FEN models is that the independent variable correlates with chain conformation, irrespective of flow. Of the FEN relationships taken from the literature, only the conformational models from Zuidema et al. [12] and Steenbakkers et al. [13] were found to be consistent with the simulation results. The nucleation rate correlated well with the first normal stress difference, but the dependence was exponential, rather than the functional forms proposed by Ziabicki [9] and Koscher and Fulchiron [10]. Our empirical approximation to the free energy model from Coppola et al. [15] was unsuccessful in capturing the trend of the data, and the strain rate-based models [7,8] were found to be fundamentally inconsistent with our results.

An investigation of the correlation of Kuhn segment conformation with the rate of nucleation led to a new set of FEN models. These models were found to provide the most accurate fits to the NEMD data, suggesting that the degree to which Kuhn segments are oriented is the best measure among those studied for the acceleration in the nucleation rate due to flow. Given that Kuhn segment orientation can be computed for some rheological models and probed experimentally through melt birefringence, these models are promising candidates for future studies. In recognition of the fact that in some cases Kuhn segment orientation data is not readily available, the Kuhn segment relationships were transformed into expressions based on the extra stress tensor under the requirement that the stress-optical rule is in effect. For our results, the extra stress-based models were found to be more accurate than those based on the first normal

stress difference, but generally less accurate than the models based on Kuhn segment conformations.

Supplementary material

The details of the force field used in this study are provided in the supplementary material.

Acknowledgements

We gratefully acknowledge financial support from the ExxonMobil Chemical Company, Baytown, TX.

Appendix Index of flow-enhanced nucleation rate models referenced in this work.

Source	**Model Type**	**Nucleation rate**	**Parameters**	**Residual [log (10^{30}m^{-3}s^{-1})]**
Liedauer et al. [7]	strain rate	$I_S = I_{S,q} + \alpha_L \dot{\gamma}^2$	-	-
Guo et al. [8]	strain rate	$I_S = I_{S,q} + \alpha_G \frac{\beta_G \dot{\gamma}^{\nu_G}}{1+\beta_G \dot{\gamma}^{\nu_G}}$	-	-
Ziabicki [9]	stress	$I_S = I_{S,q} \exp\left(\theta_Z N_1^2\right)$	$I_{S,q}$ = 86.8×10^{30}m^{-3}s^{-1} θ_{Z1} = 0.0157 MPa^{-1}	1.58
Koscher and Fulchiron [10]	stress	$I_S = I_{S,q} + \theta_{KF} N_1$	$I_{S,q}$ = 23.9×10^{30}m^{-3}s^{-1} θ_{KF} = 52.3 ×10^{30}m^{-3}s^{-1}MPa^{-1}	5.24
Doufas et al. [11]	stress/ conf.	$I_S = I_{S,q} \exp\left(\theta_D \, \mathrm{tr}(\boldsymbol{\tau})\right)$	-	-
Zuidema et al. [12]	conf.	$I_S = I_{S,q} + \theta_Z J_2 \left(\mathbf{C} - \mathbf{I}\frac{\mathrm{tr}(\mathbf{C})}{3}\right)$	$I_{S,q}$ = 55.3×10^{30}m^{-3}s^{-1} θ_{Z2} = 239×10^{30}m^{-3}s^{-1}	0.603
Steenbakkers et al. [13]	conf.	$I_S = I_{S,q} + \theta_S(\lambda^4 - 1)$	$I_{S,q}$ = 42.3×10^{30} m^{-3}s^{-1} θ_S = 136×10^{30} m^{-3}s^{-1}	0.618
Graham and Olmsted [14]	conf.	$I_S = I_{S,q} \exp\left[\theta_{GO}\left(\lambda^2 - 1\right)\right]$	$I_{S,q}$ = 86.2×10^{30} m^{-3}s^{-1} θ_{GO} = 1.17	2.62
Coppola et al. [15]	free energy	$I_S = I_{S,q}\left(1+\frac{\mu P_{2,C}^2}{\Delta G_q}\right)\exp\left[\frac{K}{T\Delta G_q^2}\left(1-\frac{1}{\left[1+\mu P_{2,C}^2/\Delta G_q\right]^2}\right)\right]$	$I_{S,q}$ = 55.5×10^{30}m^{-3}s^{-1} μ = 4.75 ×10^4 kJ mol^{-1} K = 3.51 ×10^{-4} kJ^2 K mol^{-2}	0.840

			ΔG_q = 137 kJ mol^{-1}	
this study	stress	$I_S = I_{S,q}\exp(\theta_{M1} N_1)$	$I_{S,q}$ = 47.2×10^{30}m^{-3}s^{-1} θ_{M1} = 0.255 MPa^{-1}	0.593
this study	conf.	$I_S = I_{S,q}\exp\left[\theta_{M2}\sqrt{J_2\left(\mathbf{C}_K - \mathbf{I}\frac{\mathrm{tr}(\mathbf{C}_K)}{3}\right)}\right]$	$I_{S,q}$ = 42.5×10^{30}m^{-3}s^{-1} θ_{M2} = 7.76	0.222
this study	conf.	$I_S = I_{S,q}\exp\left[\theta_{M3}\sqrt{J_2\left(\mathbf{P}_{2,K}\right)}\right]$	$I_{S,q}$ = 38.5×10^{30} m^{-3}s^{-1} θ_{M3} = 5.79	0.191
this study	conf.	$I_S = I_{S,q}\exp\left(\theta_{M4} P_{2,K}\right)$	$I_{S,q}$ = 39.9×10^{30} m^{-3}s^{-1} θ_{M4} = 7.02	0.208
this study	stress	$I_S = I_{S,q}\exp\left[\theta_{M5}\sqrt{J_2(\boldsymbol{\tau})}\right]$	$I_{S,q}$ = 39.3×10^{30}m^{-3}s^{-1} θ_{M5} = 0.275 MPa^{-1}	0.295
this study	stress	$I_S = I_{S,q}\exp\left[\theta_{M6}\tau^{(1)}\right]$	$I_{S,q}$ = 42.8×10^{30} m^{-3}s^{-1} θ_{M6} = 0.271 MPa^{-1}	0.479

References

[1] M. Doi and S.F. Edwards, *The Theory of Polymer Dynamics* (Clarendon Press, 1986).

[2] R.B. Bird, *Dynamics of Polymeric Liquids (2v.).* (Wiley, 1996).

[3] W. Schneider, A. Köppl, and J. Berger, Int. Polym. Process. **2**, 151 (1988).

[4] S. Liedauer, G. Eder, and H. Janeschitz-Kriegl, Int. Polym. Process. **10**, 243 (1995).

[5] G.W.M. Peters, L. Balzano, and R.J.A. Steenbakkers, in *Handb. Polym. Cryst.*, edited by E. Piorkowska and G.C. Rutledge (Wiley, Hoboken, 2013), pp. 399–431.

[6] R.S. Graham, Chem. Commun. **50**, 3531 (2014).

[7] S. Liedauer, G. Eder, H. Janeschitz-Kriegl, P. Jerschow, W. Geymayer, and E. Ingolic, Int. Polym. Process. **8**, 236 (1993).

[8] X. Guo, A.I. Isayev, and L. Guo, Polym. Eng. Sci. **39**, 2096 (1999).

[9] A. Ziabicki, J. Nonnewton. Fluid Mech. **30**, 157 (1988).

[10] E. Koscher and R. Fulchiron, Polymer **43**, 6931 (2002).

[11] A.K. Doufas, A.J. McHugh, and C. Miller, J. Nonnewton. Fluid Mech. **92**, 27 (2000).

[12] H. Zuidema, G.W.M. Peters, and H.E.H. Meijer, Macromol. Theory Simulations **10**, 447 (2001).

[13] R.J.A. Steenbakkers, G.W.M. Peters, H.E.H. Meijer, A. Co, G.L. Leal, R.H. Colby, and A.J. Giacomin, in *AIP Conf. Proc.* (AIP, 2008), pp. 493–495.

[14] R.S. Graham and P.D. Olmsted, Phys. Rev. Lett. **103**, 115702 (2009).

[15] S. Coppola, N. Grizzuti, and P.L. Maffettone, Macromolecules **34**, 5030 (2001).

[16] J. Baert and P. Van Puyvelde, Macromol. Mater. Eng. **293**, 255 (2008).

[17] V.A. Shneidman, J. Chem. Phys. **141**, 051101 (2014).

[18] J. Wedekind, D. Reguera, and R. Strey, J. Chem. Phys. **125**, 214505 (2006).

[19] D.A. Nicholson and G.C. Rutledge, J. Chem. Phys. **144**, 134105 (2016).

[20] G.C. Rutledge, in *Handb. Polym. Cryst.*, edited by E. Piorkowska and G.C. Rutledge (Wiley, Hoboken, 2013), pp. 197–214.

[21] M. Anwar, J.T. Berryman, and T. Schilling, J. Chem. Phys. **141**, 124910 (2014).

[22] D.A. Nicholson and G.C. Rutledge, J. Chem. Phys. **145**, 244903 (2016).

[23] P. Cassagnau, J.P. Montfort, G. Marin, and P. Monge, Rheol. Acta **32**, 156 (1993).

[24] L.J. Fetters, D.J. Lohse, D. Richter, T.A. Witten, and A. Zirkel, Macromolecules **27**, 4639 (1994).

[25] P.S. Stephanou, C. Baig, G. Tsolou, V.G. Mavrantzas, and M. Kröger, J. Chem. Phys. **132**, 124904 (2010).

[26] R. Everaers, S.K. Sukumaran, G.S. Grest, C. Svaneborg, A. Sivasubramanian, and K. Kremer, Science **303**, 823 (2004).

[27] W. Paul, D.Y. Yoon, and G.D. Smith, J. Chem. Phys. **103**, 1702 (1995).

[28] N. Waheed, M.S. Lavine, and G.C. Rutledge, J. Chem. Phys. **116**, 2301 (2002).

[29] N. Waheed, M.J. Ko, and G.C. Rutledge, Polymer **46**, 8689 (2005).

[30] D.J. Evans and G.P. Morriss, *Statistical Mechanics of Nonequilibrium Liquids* (Acadmic, London, 1990).

[31] D.J. Evans, Mol. Phys. **37**, 1745 (1979).

[32] T.A. Hunt and B.D. Todd, Mol. Phys. **101**, 3445 (2003).

[33] A.W. Lees and S.F. Edwards, J. Phys. C Solid State Phys. **5**, 1921 (1972).

[34] M. Dobson, J. Chem. Phys. **141**, 184103 (2014).

[35] T.A. Hunt, Mol. Simul. **42**, 347 (2015).

[36] S. Plimpton, J. Comput. Phys. **117**, 1 (1995).

[37] M. Tuckerman, B.J. Berne, and G.J. Martyna, J. Chem. Phys. **97**, 1990 (1992).

[38] P. Yi, C.R. Locker, and G.C. Rutledge, Macromolecules **46**, 4723 (2013).

[39] G. Ungar, J. Stejny, A. Keller, I. Bidd, and M.C. Whiting, Science **229**, 386 (1985).

[40] P. Yi and G.C. Rutledge, J. Chem. Phys. **135**, 024903 (2011).

[41] A.I. Isayev, T.W. Chan, K. Shimojo, and M. Gmerek, J. Appl. Polym. Sci. **55**, 807 (1995).

[42] A.I. Isayev, T.W. Chan, M. Gmerek, and K. Shimojo, J. Appl. Polym. Sci. **55**, 821 (1995).

[43] J.H. Irving and J.G. Kirkwood, J. Chem. Phys. **18**, 817 (1950).

[44] A.K. Doufas, A.J. McHugh, C. Miller, and A. Immaneni, J. Nonnewton. Fluid Mech. **92**, 81 (2000).

[45] A.K. Doufas and A.J. McHugh, J. Rheol. **45**, 403 (2001).

[46] A.K. Doufas and A.J. McHugh, J. Rheol. **45**, 1085 (2001).

[47] A.K. Doufas, Rheol. Acta **53**, 269 (2014).

[48] G.W.M. Peters, F.H.M. Swartjes, and H.E.H. Meijer, Macromol. Symp. **185**, 277 (2002).

[49] F.H.M. Swartjes, G.W.M. Peters, S. Rastogi, and H.E.H. Meijer, Int. Polym. Process. **18**, 53 (2003).

[50] J. van Meerveld, M. Hütter, and G.W.M. Peters, J. Nonnewton. Fluid Mech. **150**, 177 (2008).

[51] R.J.A. Steenbakkers and G.W.M. Peters, J. Rheol. **55**, 401 (2011).

[52] A.I. Leonov, J. Nonnewton. Fluid Mech. **42**, 323 (1992).

[53] F.J.M.F. Custódio, R.J.A. Steenbakkers, P.D. Anderson, G.W.M. Peters, and H.E.H. Meijer, Macromol. Theory Simulations **18**, 469 (2009).

[54] T.B. van Erp, P.C. Roozemond, and G.W.M. Peters, Macromol. Theory Simulations **22**, 309 (2013).

[55] P.C. Roozemond and G.W.M. Peters, J. Rheol. **57**, 1633 (2013).

[56] R.J.A. Steenbakkers and G.W.M. Peters, J. Rheol. **55**, 401 (2011).

[57] A.J. McHugh, J. Appl. Polym. Sci. **19**, 125 (1975).

[58] A.J. McHugh, Polym. Eng. Sci. **22**, 15 (1982).

[59] A. Ziabicki, Colloid Polym. Sci. **274**, 705 (1996).

[60] S. Acierno, S. Coppola, N. Grizzuti, and P.L. Maffettone, Macromol. Symp. **185**, 233 (2002).

[61] S. Acierno, S. Coppola, and N. Grizzuti, J. Rheol. **52**, 551 (2008).

[62] R. Zheng and P.K. Kennedy, J. Rheol. **48**, 823 (2004).

[63] K.H. Kim, A.I. Isayev, and K. Kwon, J. Appl. Polym. Sci. **95**, 502 (2005).

[64] K. Jolley and R.S. Graham, Rheol. Acta **52**, 271 (2013).

[65] F.E. Bernardin and G.C. Rutledge, Macromolecules **40**, 4691 (2007).

[66] J. van Meerveld, G.W.M. Peters, and M. Hütter, Rheol. Acta **44**, 119 (2004).

[67] D.W. Mead and L.G. Leal, Rheol. Acta **34**, 339 (1995).

[68] G. Strobl, *The Physics of Polymers* (Springer Berlin Heidelberg, New York, 2007).

[69] A.S. Lodge, Trans. Faraday Soc. **52**, 120 (1956).